Publications of the Astronomical Society of Australia (PASA), Vol. 34, e021, 10 pages (2017).

doi:10.1017/pasa.2017.16

PKS 1954–388: RadioAstron Detection on 80,000 km Baselines and Multiwavelength Observations

P. G. Edwards[1,20], Y. Y. Kovalev[2], R. Ojha[3,4,5], H. An[6,7], H. Bignall[1], B. Carpenter[3,4], T. Hovatta[8,9], J. Stevens[1], P. Voytsik[2], A.S. Andrianov[2], M. Dutka[3,4], H. Hase[10], S. Horiuchi[11], D. L. Jauncey[1,12], M. Kadler[13], M. Lisakov[2], J. E. J. Lovell[14], J. McCallum[14], C. Müller[15], C. Phillips[1], C. Plötz[12], J. Quick[16], C. Reynolds[1], R. Schulz[17], K. V. Sokolovsky[2,18,19], A. K. Tzioumis[1] and V. Zuga[2]

[1]CSIRO Astronomy and Space Science, PO Box 76, Epping, NSW 1710, Australia
[2]Astro Space Center of Lebedev Physical Institute, Profsoyuznaya 84/32, 117997 Moscow, Russia
[3]NASA, Goddard Space Flight Center, Greenbelt, MD 20771, USA
[4]Catholic University of America, Washington, DC 20064, USA
[5]University of Maryland, Baltimore County, 1000 Hilltop Cir, Baltimore, MD 21250, USA
[6]Kavli Institute for Particle Astrophysics and Cosmology, Stanford University, Stanford, CA 94305, USA
[7]Department of Astronomy and Space Science, Chungbuk National University, Cheongju 28644, Republic of Korea
[8]Aalto University Metsähovi Radio Observatory, Metsähovintie 114, FL-02540 Kylmälä, Finland
[9]Aalto University Department of Radio Science and Engineering, PO Box 13000, FI-00076 Aalto, Finland
[10]Bundesamt für Kartographie und Geodäsie, 93444 Bad Kötzting, Germany
[11]CSIRO Astronomy and Space Science, Canberra Deep Space Communication Complex, ACT 2901, Australia
[12]Research School of Astronomy and Astrophysics, Australian National University, Canberra, ACT 2611, Australia
[13]Lehrstuhl für Astronomie, Universität Würzburg, 97074 Würzburg, Germany
[14]School of Physical Sciences, University of Tasmania, Private Bag 37, Hobart, TAS 7001, Australia
[15]Department of Astrophysics/MAPP, Radboud University Nijmegen, PO Box 9010, 6500 GL Nijmegen, The Netherlands
[16]Hartebeesthoek Radio Astronomy Observatory, Krugersdorp 1740, South Africa
[17]ASTRON, the Netherlands Institute for Radio Astronomy, PO Box 2, 7990 AA Dwingeloo, The Netherlands
[18]IAASARS, National Observatory of Athens, 15236 Penteli, Greece
[19]Sternberg Astronomical Institute, Moscow State University, 119992 Moscow, Russia
[20]Email: Philip.Edwards@csiro.au

(Received January 27, 2017; Accepted March 24, 2017)

Abstract

We present results from a multiwavelength study of the blazar PKS 1954–388 at radio, UV, X-ray, and gamma-ray energies. A RadioAstron observation at 1.66 GHz in June 2012 resulted in the detection of interferometric fringes on baselines of 6.2 Earth-diameters. This suggests a source frame brightness temperature of greater than 2×10^{12} K, well in excess of both equipartition and inverse Compton limits and implying the existence of Doppler boosting in the core. An 8.4-GHz TANAMI VLBI image, made less than a month after the RadioAstron observations, is consistent with a previously reported superluminal motion for a jet component. Flux density monitoring with the Australia Telescope Compact Array confirms previous evidence for long-term variability that increases with observing frequency. A search for more rapid variability revealed no evidence for significant day-scale flux density variation. The ATCA light-curve reveals a strong radio flare beginning in late 2013, which peaks higher, and earlier, at higher frequencies. Comparison with the *Fermi* gamma-ray light-curve indicates this followed ∼9 months after the start of a prolonged gamma-ray high-state—a radio lag comparable to that seen in other blazars. The multiwavelength data are combined to derive a Spectral Energy Distribution, which is fitted by a one-zone synchrotron-self-Compton (SSC) model with the addition of external Compton (EC) emission.

Keywords: galaxies: active – galaxies: jets – gamma rays: galaxies – ISM: structure – radio continuum: galaxies

1 INTRODUCTION

A major challenge in astronomy is the struggle to observe objects with an angular resolution sufficient to probe the underlying physical mechanisms. The longer wavelengths of radio-astronomy initially made the quest for high angular resolution more difficult, but the relative ease of preserving phase information enabled the technique of Very Long Baseline Interferometry (VLBI). Intercontinental VLBI routinely achieves milli-arcsecond–scale angular resolutions, and

extending the baselines between telescopes into space, with satellite-based telescopes, currently yields the highest angular resolution achieved in astronomy.

In this paper, we describe multi-wavelength studies of PKS 1954–388 with the Australia Telescope Compact Array (ATCA, maximum baseline 6 km), and present a second-epoch 8.4 GHz TANAMI (Tracking Active Galactic Nuclei with Austral Milliarcsecond Interferometry) VLBI image (maximum baseline ∼10,000 km) and a 1.66-GHz RadioAstron Active Galactic Nuclei (AGN) Survey observation (maximum baseline ∼80,000 km, or 6.2 Earth-diameters). The pronounced variability of the source at radio and gamma-ray energies is examined, and we combine these with data from the *Swift* and *Fermi* satellites to obtain a Spectral Energy Distribution (SED) for the source which is fitted by a self-consistent model.

2 PKS 1954–388

PKS 1954–388 was first catalogued in the Parkes 2.7-GHz survey (Shimmins 1971). The source was observed in May 1969 with a flux density of 2.00 ± 0.05 Jy and again in June 1970 with a flux density of 1.50 ± 0.05 Jy, and noted as being possibly variable. A comparison with the Molonglo 408 MHz catalog indicated an inverted spectrum, prompting follow-up optical observations with the Mt Stromlo 74 inch (1.9 m) telescope yielding an identification with an 18th magnitude galaxy (Shimmins et al. 1971). Early observations with the 3.9 m Anglo-Australian Telescope gave a redshift of $z = 0.63$ (Browne, Savage, & Bolton 1975).

The discovery of a high level of optical polarisation, 11%, by Impey & Tapia (1988) led to classification of the source as a blazar. Oshlack, Webster, & Whiting (2002) used measurements of the Hβ line width and luminosity to estimate a central black hole mass of $4.3 \times 10^8 M_\odot$ for the source.

PKS 1954–388 was not detected by the EGRET instrument on the *Compton Gamma-Ray Observatory*. However, the radio properties led Vercellone et al. (2004) to classify the source as a candidate gamma-ray AGN, a prediction borne out by the detection of the source with the *Fermi* Large Area Telescope (Abdo et al. 2010). Studies by Nolan et al. (2012) indicate the source is variable at gamma-ray energies, with a $<1\%$ chance of the flux being steady, behaviour common to the AGN class.

The source was included in the VSOP (VLBI Space Observatory Programme) AGN Survey (Hirabayashi et al. 2000) though it was not observed before the end of the mission. Inclusion in the survey list did, however, result in the source being part of the multi-epoch monitoring program with the ATCA at 1.4, 2.5, 4.8 and 8.6 GHz between 1996 October and 2000 February. This revealed pronounced variability at the higher frequencies but no evidence at 1.4 GHz for any variability on time scales of ∼70 d (Tingay et al. 2003).

A series of VLBI observations—at 4.9 GHz in 1993 May (Shen et al. 1998), at 4.9 GHz in 1996 June (Fomalont et al. 2000), at 15 GHz in 1998 June (Kovalev et al. 2005), and at 2.3 and 8.6 GHz in 2002 December (Pushkarev & Kovalev 2012)—found the source to be strongly core dominated (see also Pusharev & Kovalev 2015). A deeper VLBI observation at 8.4 GHz in 2002 July detected, in addition to the core, a marginally significant second component ∼2.8 mas to the west (Ojha et al. 2004).

Piner et al. (2012) used 36 epochs of Radio Reference Frame VLBI observations at 8 GHz between 1994 and 2003 to measure apparent speeds for two jet components. Both components displayed motions of ∼0.1 mas yr^{-1}, with corresponding apparent speeds of 3.7 ± 1.8 c and 3.7 ± 1.0 c for the fainter, outer and brighter, inner components, respectively. The outer component of Piner et al. (2012) is consistent with the weak secondary component of Ojha et al. (2004).

PKS 1958–388 is part of the multi-epoch TANAMI program and a first epoch 8.4 GHz image from 2008 February is presented by Ojha et al. (2010). A jet extends over ∼5 mas to the west, and a source frame brightness temperature of 1.5×10^{12} K was derived for the core. Böck et al. (2016) report a source frame brightness temperature of 2.2×10^{11} K for a subsequent TANAMI observation in 2008 November, indicating significant variability. The brightness temperature is the surface brightness of a radio source expressed for convenience in terms of the equivalent black body temperature. It is an important parameter as there are limits on the intrinsic brightness temperature imposed by both Inverse-Compton cooling and equipartition arguments—see, e.g., Kellermann (2002) for a review. As the measurable maximum brightness temperature depends on baseline length, the best way to constrain measurements is to extend VLBI baselines beyond the Earth's surface with an element in space. The RadioAstron mission achieved this with the launch of the Spektr-R satellite on 2011 July 18, with observations at 0.3, 1.6, 4.8 and 22 GHz being routinely conducted (Kardashev et al. 2013).

3 OBSERVATIONS

3.1. RadioAstron

A RadioAstron AGN Survey Program observation of PKS 1954–388 was made at 1.66 GHz on 2012 August 23 with observation code raes03br. The snap-shot mode observation started at 15:45 UT and lasted 1 h using the Spektr-R satellite[1] and the Parkes 64 m and Mopra 22 m telescopes. At 1.66 GHz, the satellite formats RCP data with 16-MHz bandwidths, which are 1-bit sampled. A parity bit is added for each byte and the data transmitted to the Earth at 144 Mbps. The ground telescopes record data in two, dual-polarisation, 16-MHz bandwidth IF bands, with 2-bit sampling of the data yielding a data rate of 256 Mbps.

Data from the spacecraft were transmitted in real time to the Pushchino tracking station and recorded to disk. Data

[1] The 1.6-GHz receiver on the satellite was designed by the CSIRO Division of Radiophysics with the support of CSIRO Office of Space Science and Applications and manufactured by British Aerospace Australia, with the low-noise amplifier built by Mitec, Ltd., Australia.

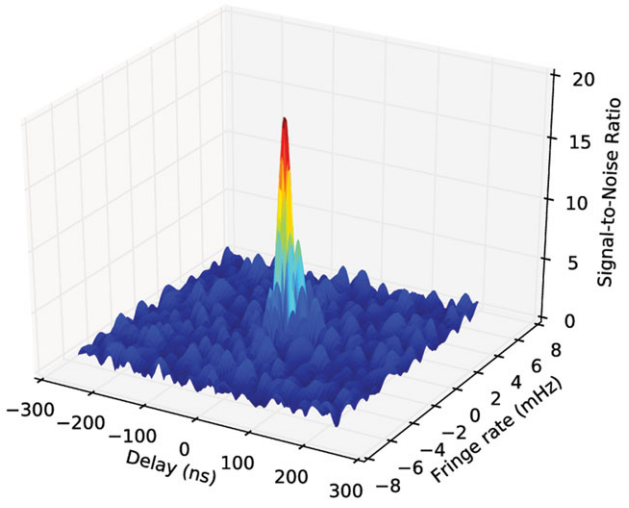

Figure 1. The detection of fringes at 1.66 GHz in (delay, delay-rate) space for PKS 1954–388 between the Parkes 64 m telescope and the RadioAstron satellite, Spektr-R.

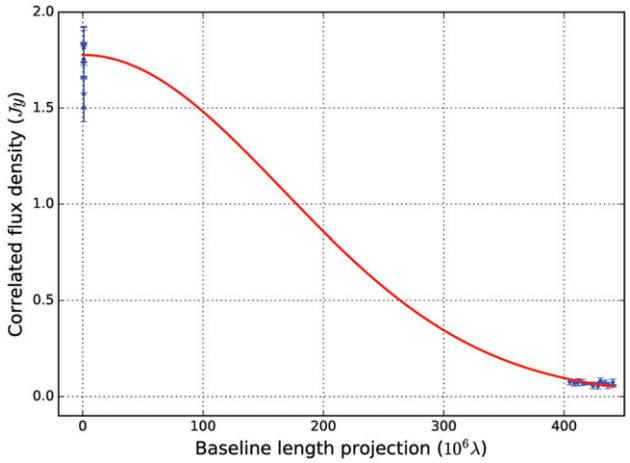

Figure 2. Plot of the correlated flux density as a function of baseline length for PKS 1954–388 at 1.66 GHz. Blue points are the data: the inner points correspond to the Parkes–Mopra baseline, the outer points are the baselines to the RadioAstron satellite, Spektr-R The red curve is the simplest Gaussian model-fit—see text for details.

from the ground radio telescopes were recorded to disk and later reformatted to Mark 5B format before being electronically transferred to the Astro Space Centre (ASC). The data were correlated at the ASC correlator (Kardashev et al. 2013), with clear fringes being found at 1.6 GHz between the three telescopes (see Figure 1). The data were exported from the correlator and fringe-fit in the software package PIMA (Petrov et al. 2011). The (u, v)-coverage for the observation is, as expected for this snap-shot mode, very sparse, with the projected Parkes–Mopra baseline being $\sim$1 Mλ and the baselines to the spacecraft ranging from 403 to 440 Mλ, 5.8 to 6.2 Earth-diameters, at a position angle of $\sim 177^\circ$. The goal of the AGN Survey is to determine whether sources are detectable over a range of baseline lengths and use this information to infer angular sizes and corresponding brightness temperatures.

Initially, the amplitudes and signal-to-noise ratios (SNRs) were plotted as a function of integration time for each baseline on each scan in order to estimate the coherence time. For this observation, no significant losses were evident with up to 10 min integration time. Space VLBI fringes were detected in 10 min integration times with SNRs of $\sim$20 on the baselines to Parkes, and SNRs of $\sim$7 on the baselines to Mopra, corresponding to a probability of false detection on SVLBI baselines significantly less than 10^{-6}.

A correlated flux density of 1.78 Jy was measured on the Parkes–Mopra baseline, and $\sim$0.07 Jy on Earth–space baselines. The simplest model-fit to the data is with single circular Gaussian component with a total flux density of 1.78 Jy and full-width half-maximum (FWHM) of 0.47 mas (see Figure 2). A circular Gaussian component was adopted for simplicity, although the size is tightly constrained in the north–south direction but poorly determined in the east–west direction. Following Kovalev et al. (2005), we calculate an observer's frame brightness temperature of 3.6×10^{12} K for this model. The limited (u, v)-coverage means we cannot be certain that fitting a single Gaussian model-component to the ground-ground and ground-space data is the correct approximation, and in fact it is highly likely that the north–south Parkes–Mopra baseline is sampling some of the jet structure to the west of the core (see Sections 2 and 3.2). However, there is a very conservative minimum brightness temperature associated just with the ground-space data: Following Lobanov (2015), we calculate a formal minimum observer's frame brightness temperature of 1.3×10^{12} K. These values must be multiplied by $(1+z)$ to obtain the corresponding source frame brightness temperatures. Incorporating the expected calibration uncertainties, the simple fit, which effectively provides an upper limit, yields a source frame brightness temperature of $(6\pm1)\times10^{12}$ K and the minimum source frame brightness temperature is 2×10^{12} K, respectively.

3.2. TANAMI

An 8.4 GHz TANAMI observation was made on 2012 September 16, less than a month after the RadioAstron observation. Participating in this observation were the 'tied array' of five 22 m ATCA antennas, a single 12 m ASKAP (Australian Square Kilometre Array Pathfinder) antenna with a single pixel feed, the Ceduna 30 m, Hartebeesthoek 26 m, Hobart 26 m, Parkes 64 m, Tidbinbilla 70 m, TIGO 6 m telescopes, and the 12 m Katherine telescope of the AuScope array (Lovell et al. 2013).

PKS 1954–388 was observed in six $\sim$10 min snapshots over a period of 9 h to build up good (u, v)-coverage. The source had not risen at Hartebeesthoek (in South Africa) for the first three scans and had set at the TIGO site (in Concepcion, Chile) for the last three scans. The resulting image is shown in Figure 3.

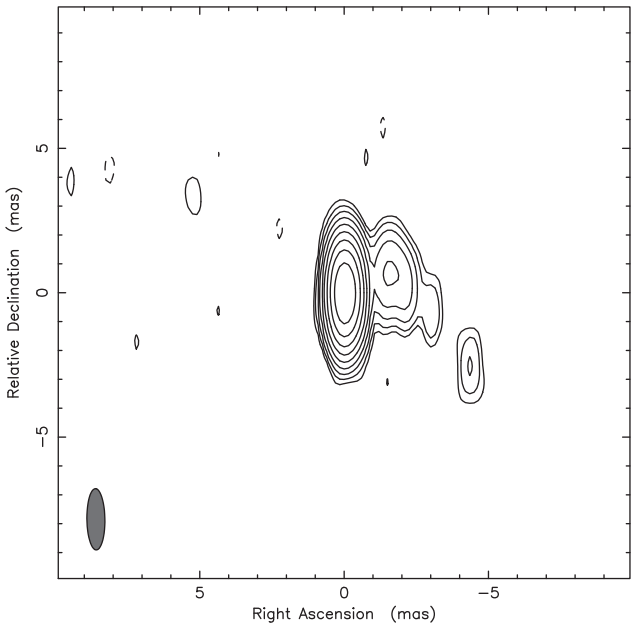

Figure 3. TANAMI image from an 8.4-GHz observation on 2012 September 16. The image peak is 1.29 Jy/beam, and the beam (FWHM) is 2.1 mas × 0.6 mas at a position angle of 1°. Contour levels are –0.2% (dashed), 0.2%, 0.4%, 0.8%, 1.6%, 3.2%, 6.4%, 12.8%, 25.6% and 51.2% of the peak.

Model-fitting of this TANAMI observation yields a 1.5 Jy core, an 85 mJy component at 1.7 mas from the core at a position angle of −67°, and a 42 mJy component at 2.1 mas and a position angle of −101°. There is also about 11 mJy of flux 5 mas from the core and a position angle of −120°. This morphology is consistent with previous VLBI images in Ojha et al. (2004), Ojha et al. (2010) and Piner et al. (2012), all of which report a bright core and a westward jet.

The innermost component is readily identifiable with the innermost component of Piner et al. (labelled 2 in their Table 5) given the similarity in intensity, position angle and extrapolated core distance. The other components do not lie at the extrapolated distance (∼3.2 mas) of the outer Piner et al. component. Given the sparse (u, v)-coverage of the Radio Reference Frame observations for sources as far south as PKS 1954–388, the complex jet morphology, and the large gap in observing epochs, the details of proper motion are an open question to be resolved by further TANAMI monitoring.

3.3. ATCA

PKS 1954–388 has been regularly observed with the ATCA as part of the flux density calibration monitoring program (C007) and also as part of a multi-frequency program (C1730) monitoring TANAMI and other gamma-ray sources (Stevens et al. 2012). Prior to the Compact Array Broadband Backend (CABB: Wilson et al. (2011)) upgrade in 2009, C007 observations were made with 128 MHz bandwidths centred at 4.8 and 8.6, 18.5 and 19.5 GHz. In the CABB era, C1730 observations are made with 2 GHz bandwidths centred at 5.5 and

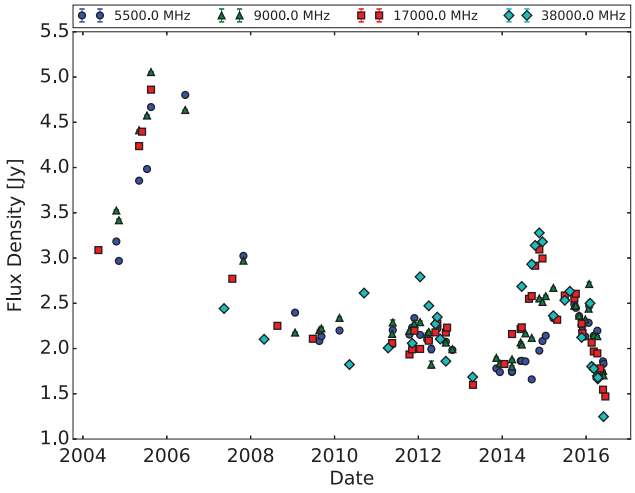

Figure 4. The radio light-curve derived from ATCA monitoring data—see text for details.

9, 17 and 19, and 38 and 40 GHz. Observations at 38 and 40 GHz commenced in early 2007. The observations are made in snap-shot mode, with integrations of several minutes in each pair of bands. Observations at 38 and 40 GHz are preceded by a 'pointing' scan on a bright source (on occasions, PKS 1954–388 itself) to update the pointing model for that area of sky. PKS 1934–638 is used as primary flux density calibrator (Partridge et al. 2016), with Uranus also used in the 7-mm band in more compact array configurations. Errors are dominated by systematic effects and are estimated to be less than 5% below 10 GHz, and up to 10% at 40 GHz. The data presented in this paper are incorporated in the ATCA calibrator database,[2] which provides a flux density model of each source in each observed band for each epoch. This allows us to compute the flux density at the same frequency regardless of the centre frequency that was actually observed in a particular epoch.

The resulting light-curve in four frequency bands is shown in Figure 4. The source is obviously quite variable and in a high-state in 2005–2006. From 2007 to 2013, the source showed some irregular variations from epoch to epoch, which is undersampled by our observations, but overlaid on a general decline in flux density. We note that the 2012 August RadioAstron observation was made when the source was in a relatively quiescent radio state. At the end of 2013, the source underwent another outburst. In this instance, the source was monitored in all three frequency bands and, as shown in Figure 5 (an expansion of a sub-range of Figure 4), the radio flare proceeds earlier, and more rapidly at higher frequencies.

As mentioned in Section 2, PKS 1954–388 was monitored at four frequencies over 16 epochs by Tingay et al. (2003). The source was in a high state (∼5 Jy at 8.4 GHz, with an inverted spectrum) in October 1996 however was at its lowest levels (∼1 Jy at all frequencies) in February 2000. Tingay

[2] http://www.narrabri.atnf.csiro.au/calibrators/

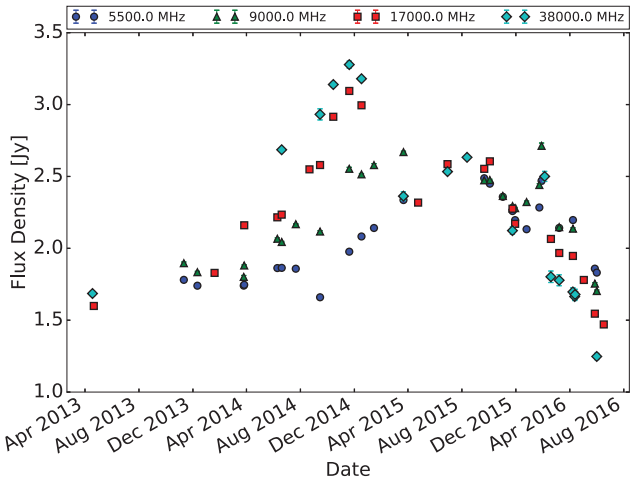

Figure 5. A subset of the ATCA monitoring data in Figure 4 with an expanded time axis to more clearly see the frequency dependence of the flare that commenced at the end of 2013.

et al. (2003) characterised the variability of sources monitored at multiple epochs with a variability index defined as the RMS variation from the mean flux density, divided by the mean flux density. PKS 1954–388 had variability indices of 0.11 at 1.4 GHz, 0.16 at 2.5 GHz, 0.26 at 4.8 GHz, and 0.30 at 8.6 GHz. The variability index at 8.4 GHz was in the top 10% of the sample of 185 sources.

We undertake a similar analysis for the ATCA data presented here. In order to make a comparison between frequencies, we only use the data points after the installation of the 7 mm receivers in 2007, and as a consequence omit the data from the large flare in 2005–2006.

PKS 1954–388 had variability indices of 0.13 at 5.5 GHz (29 data points), 0.12 at 9.0 GHz (29 data points), 0.16 at 17 GHz (25 data points) and 0.19 at 38 GHz (20 data points). While the absolute values obviously differ, the general trend of the variability index increasing with frequency persists.

3.3.1. Search for short timescale variability with the ATCA

PKS 1954–388 was also observed with the ATCA as part of project C2898 (Monitoring of RadioAstron AGN Survey targets to measure intra-day and longer term variability). Short timescale variability at a range of GHz frequencies potentially provides information on the scattering properties of the local Galactic interstellar medium (ISM) along the line of sight. PKS 1954–388 was observed in approximately 10 scans at each of several frequencies between 1 and 20 GHz, with irregular sampling over a 15-d period in 2014 June. It was also observed as part of the same project several times between 2014 July and September.

For the purposes of searching for short time-scale variability, since we are not limited by signal-to-noise, a section of each frequency band was selected that appeared to be relatively free of interference and other problems. Only the upper part of the 1–3 GHz band was selected for analysis, due to the lower frequencies being heavily affected by radio-frequency interference in the data from June 2014; the ATCA was in a compact configuration *(EW352)* at this time. The band selection was identical for all epochs. Bandpass, amplitude gain and polarization leakage corrections were determined for each day of observations using several minutes of data on the ATCA primary calibrator, PKS 1934–638. Since PKS 1954–388 is a bright, isolated point source at the ATCA, the flux density was estimated by averaging the visibilities over all baselines after applying phase-only self-calibration.

Table 1. Results of search for short-term variation with the ATCA over 15 d in 2014 June.

ν (GHz)	Bandwidth (MHz)	$\bar{S}$ (Jy)	S_{RMS} (Jy)	μ
2.75	500	1.613	0.025	0.016
4.8	400	1.832	0.022	0.012
8.8	1,000	2.034	0.022	0.011
17.0	2,000	2.295	0.031	0.014
19.0	2,000	2.307	0.029	0.013

Table 1 shows central frequency, bandwidth used, mean flux density $\bar{S}$ and RMS of the flux density measurements in June, averaged over 1-min intervals and over all channels in the selected frequency range, and the variability index as defined previously, $\mu = RMS/\bar{S}$.

During the ATCA observations in 2014 June, PKS 1954–388 showed RMS variations no larger than 1.6%, or 30 mJy, on timescales between minutes and days in the frequency range 2.5–20 GHz. These variations are not significantly larger than those determined for other sources observed in 2014 June, or than the systematic uncertainties determined by comparing data on different baselines. We assume the observed variations here represent upper limits on the true variability. A significant, ∼5–10%, decrease in flux density was observed over a 10-d period in 2014 July, over a broad bandwidth between 2 and 20 GHz, with the largest change around 5 GHz. Such a change could be consistent with interstellar scintillation of a compact component, but with only two independent data points in this time period it is not possible to constrain the variability mechanism. The spectrum became significantly more inverted in 2014 September, with a drop in flux density at frequencies below 7 GHz and an increase at frequencies above 8 GHz. This period is associated with a flare at higher frequencies seen in the longer-term ATCA monitoring data (see Figure 5).

3.4. *Swift*

We have analysed archival *Swift* (Gehrels et al. 2004) data in order to better characterise the SED of PKS 1954–388. The X-Ray Telescope (XRT; Burrows et al. 2004) on board the *Swift* spacecraft is a grazing incidence telescope with an effective area of 110 cm^2, a field of view of 23.6 arcmin and

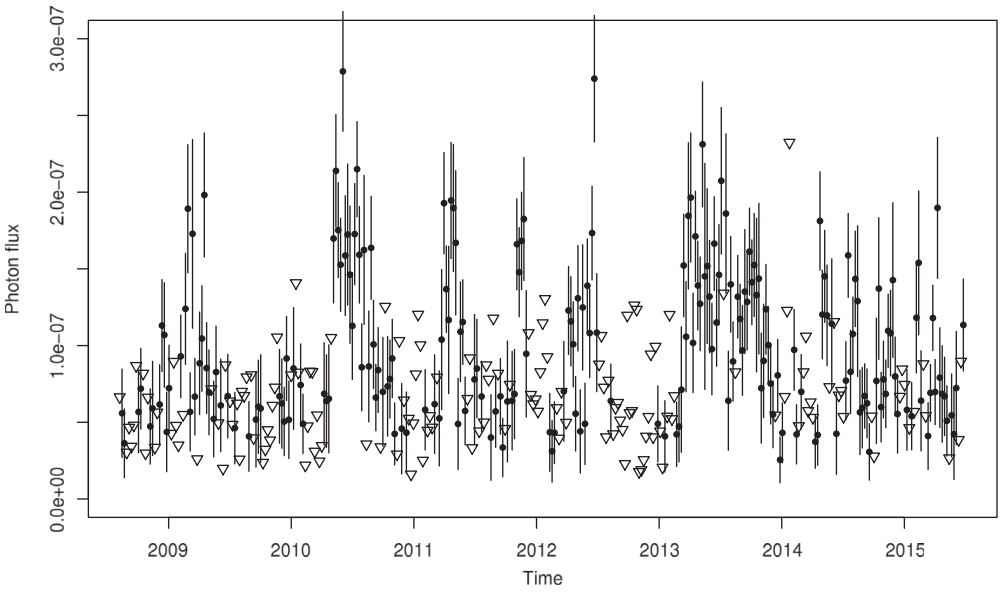

Figure 6. *Fermi* light-curve with one-week bin width. Photon fluxes are plotted in units of cm^{-2} s^{-1}. Inverted triangles denote 2σ upper limits—see text for details.

0.2–10 keV energy range. It observed PKS 1954–388 on 2007 July 31 for 5.911 ks.

The UltraViolet and Optical Telescope (UVOT; Roming et al. 2004) is a 30-cm UV/optical telescope co-aligned with the XRT covering the 170–650 nm range in a $17' \times 17'$ field. The UVOT observed PKS 1954–388 on 2010 April 9 for 1.184 ks.

The XRT data were processed using the `xrtpipeline` and the spectrum was fit using `XSpec`, both a part of the `HEASoft` package (v.6.12). A circular region with a radius of 20 pixels was used to extract the source events while a background region with a 50 pixel radius accounted for background events. The spectrum had >200 counts and so was fitted using chi-squared statistics. The spectrum was fit in the 0.3–10 keV region using an absorbed power law. The N_H column density was set to be 6.43×10^{20} cm^{-2} (Kalberla et al. 2005). The ancillary response files were generated with `xrtmkarf`.

The UVOT data were reduced using the `uvotsource` task, also a part of the `HEASoft` package (v.6.12). Source counts were extracted from a circular region with a 10-pixel radius, the background was extracted from a circular region with a 30-pixel radius.

3.5. *Fermi*

The gamma-ray data were obtained with the Large Area Telescope (LAT) aboard *Fermi*, which observes the entire sky every 3 h at energies of 0.03–300 GeV (Atwood et al. 2009). The publicly available Pass 8 data[3] were analysed using the *Fermi* ScienceTools software package version v10r0p5. We used the instrument response functions P8R2_SOURCE_V6, Galactic diffuse emission model 'gll_iem_v06.fits' and isotropic background model[4] 'iso_P8R2_SOURCE_V6_v06.txt'. Following the LAT data selection recommendations,[5] we select photons in the event class 128 and use a zenith angle cut of 90°.

Photon fluxes in the 0.1–300 GeV energy range were calculated using unbinned likelihood analysis and the tool 'gtlike' with a Minuit optimizer. We used a 7-d binning in the light-curves and calculated a 2σ upper limit if the test statistic (TS) value was less than 4 (e.g., Abdo et al. 2011). The source model was generated with the tool[6] 'make3FGLxml.py' with all sources within 20° of PKS 1954–388 included in the model with their spectral parameters, except the flux, frozen to the values determined in the 3rd *Fermi* LAT catalog (3FGL; Acero et al. 2015). For sources more than 10° from PKS 1954–388, we also froze the fluxes to the 3FGL values.

The resulting light-curve is shown in Figure 6. The data in the figure span 2008 August 8 to 2015 June 30. There are 360 week-long bins over this period. Significant fluxes were measured for 210 weeks, with upper limits derived for the remaining 150 weeks.

Until early 2013, the photon flux can be characterised as having short periods of enhanced flux with longer periods of quiescent flux. There is a ∼4 week flare in 2009 March, a ∼12 week flare starting in 2010 May, a ∼9 week flare in 2011 April/May, a ∼4 week flare in 2011 November, and a ∼12 week flare starting in 2012 April. It is notable that the onsets for the second and fourth flares are more rapid than revealed by the 7-d bin-width. There are several periods

[3] http://fermi.gsfc.nasa.gov/ssc/data/

[4] http://fermi.gsfc.nasa.gov/ssc/data/access/lat/BackgroundModels.html

[5] http://fermi.gsfc.nasa.gov/ssc/data/analysis/documentation/Cicerone/Cicerone_Data_Exploration/Data_preparation.html

[6] https://fermi.gsfc.nasa.gov/ssc/data/analysis/user/

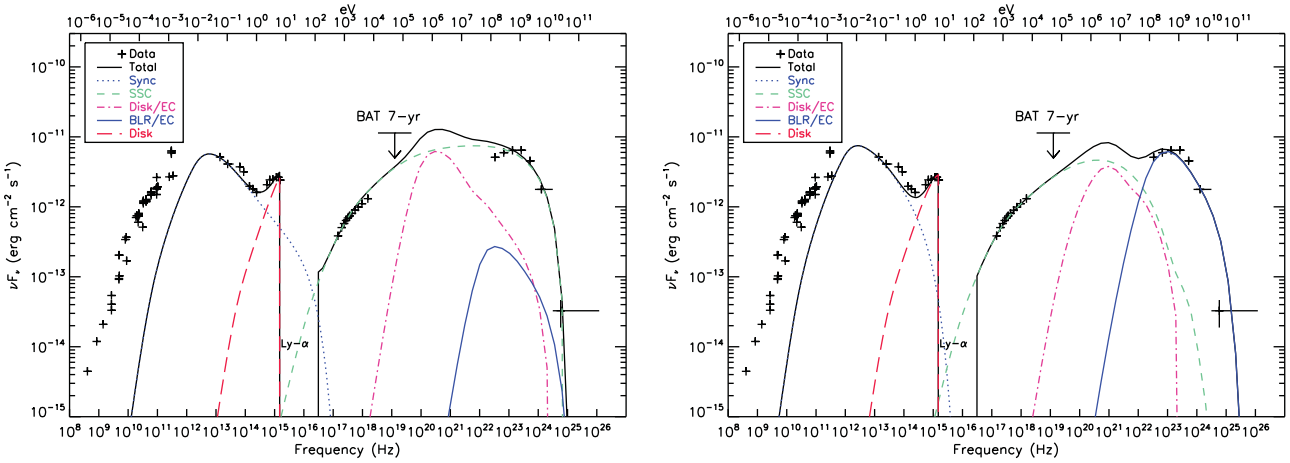

Figure 7. The observed SED and the models. The SED is measured in several radio bands, *Swift*/XRT, and *Fermi*. Infrared data are taken from the *WISE* and *2MASS* catalogs. We also show the *Swift*/BAT 7-yr sensitivity. Left: a model with the high-energy SED fit with SSC emission (model A). Right: a model with the high-energy SED fit with EC of BLR photons (model B). In these figures, the measured SED is plotted with crosses and the best-fit model is the black solid line. Individual model components are also shown: the blue dotted line is the synchrotron component, red dashed line is the direct disk component, pink dot-dashed line is the EC of the disk photons, blue triple-dot-dashed line is the EC of BLR photons and the cyan dashed line is the SSC component.

containing a series of upper limits—late 2009, early 2010, the beginning of 2011, beginning of 2012 and late 2012—during which the average weekly photon flux drops below a significant detection.

The behaviour from 2013 March onwards has been quite different. An outburst (again with a rapid onset) started in mid-March and persisted until the end of that year. For the 18 months since then the state has changed much more frequently. It is tempting to postulate that this changed behaviour is an effect of the prolonged 2013 high state. We discuss this further in Section 4.3.

3.6. SED

We combine the data from the previous sections with other multiwavelength data to derive the broadband SED and model it using one-zone synchrotron-self-Compton (SSC) emission of an electron/positron component with an addition of external Compton (EC) emission (Böttcher, Mause, & Schlickeiser 1997). In this model, the e^-/e^+ component is injected and propagates along the jet axis for a specified time period. While propagating, the particles lose their energy via synchrotron radiation and inverse-Compton upscattering. The seed photons for the inverse-Compton upscattering are the synchrotron radiation of the electrons themselves (SSC), and the emission of the Shakura-Sunyaev disk (Shakura & Sunyaev 1973) and the broad-line region (EC). We follow the component for 10^7 s ($l = 3 \times 10^{17}$ cm), calculate the integrated spectrum, and match the resulting SED with the observed one. We show our models and the parameters in Figure 7 and Table 2. Note that the data are not acquired contemporaneously. The *Fermi* data used here are the average fluxes for the period from 2008 August 4 to 2015 October 9.

Table 2. Model parameters for the observed SED.

Parameter	Symbol	Model A	Model B
Redshift	z	0.63	0.63
Bulk Lorentz factor	Γ	3	5
Viewing angle (deg.)	θ_v	5	5
Magnetic field (G)	B	1.5	0.4
Comoving radius of component (cm)	R'_b	6×10^{14}	2.6×10^{14}
Initial electron spectral index	p_1	2	1.9
Initial minimum electron Lorentz factor	$\gamma'_{\rm min}$	1×10^3	1.4×10^3
Initial maximum electron Lorentz factor	$\gamma'_{\rm max}$	3×10^4	9×10^3
Injection height (pc)	$h_{\rm inj}$	0.04	0.18
Disk luminosity (erg s^{-1})	$L_{\rm disk}$	3×10^{49}	2.3×10^{49}
Mass of the black hole ($M\odot$)	$M_{\rm BH}$	5×10^8	1.5×10^9
Accretion efficiency	η	0.03	0.03

The model parameters are not well constrained because the parameters are covariant. Hence, a different set of parameters may also be able to describe the observed SED reasonably. Furthermore, the SED is not a contemporaneous one, and large variability of blazars prevents us from inferring the parameters accurately. Nevertheless, we find that the SED is well described with a typical electron injection spectrum having a power-law index of $p \sim 2$. In the model, the optical ($\sim 10^{13} - 10^{14}$ Hz) and the X-ray spectra are the synchrotron and the SSC component, respectively. Then, simple extension of the SSC component to higher energy explains the *Fermi* spectrum reasonably (Figure 7, left), and the EC components do not play a significant role in the *Fermi* LAT band, being distinguishable only in the MeV band. Because the EC emission of the disk photons has a different shape from the observed high-energy SED, we need to suppress this by

using relatively large magnetic field (B), a small bulk Lorentz factor (Γ) and placing the base of the jet far from the black hole ($h_{\rm inj}$). The radio emission is assumed to be from a separate self-absorbed zone; hence, the model does not explain the radio data. However, radio data may provide important insights into understanding blazars via variability studies.

We also show an alternative model in Figure 7 (right), where we use the EC of broad-line region (BLR) photons to explain the *Fermi* SED. In this case, the jet base needs to be farther from the disk to suppress the disk EC emission. The magnetic-field strength for this model is lower, and the SSC emission at higher energies is suppressed. The data fit both models to within the measurement and modelling uncertainties, and thus we cannot reasonably prefer one model over the other. Obtaining a contemporaneous SED and/or monitoring spectral variability may help to distinguish between the models. This has recently been achieved by Krauß et al. (2016), who derive an SED for the relatively quiescent period from late 2008 to early 2010 and compare it with an SED from a more active period from mid-2010 to mid-2011, though without fitting a physical model to the SEDs.

4 DISCUSSION

4.1. Brightness temperature and scattering

The lower limit to the source frame brightness temperature of 2×10^{12} K is well in excess of the equipartition brightness temperature limit of $\sim 5\times10^{10}$ K (Readhead 1994) and the inverse Compton limit of $\sim 10^{11.5}$ K (Kellermann & Pauliny-Toth 1969; Readhead 1994), implying minimum Doppler factors of 40 (equipartition) and 6 (inverse Compton). The Lorentz factor of 5 and angle to the line of sight of 5° used in Model B of the SED fitting (Section 3.6) implies a Doppler factor of ∼9, and is therefore consistent with the inverse Compton Doppler factor and with the reported apparent speed of $\sim 3.7c$ (Section 2). The equipartition Doppler factor is much more difficult to reconcile.

It is necessary though to consider the impact of scattering of the source by the ISM. The simple circular Gaussian modelling of the RadioAstron observations of PKS 1954–388 used in Section 3.1 yields a core size of 0.47 mas, and if we assume that only a fraction of the flux density on the Parkes–Mopra baseline (but all of that on the space baselines) corresponds to the core, this would result in an even more compact core. The fitted angular size is remarkably consistent with the angular broadening predicted by the NE2001 model for Galactic electron density (Cordes & Lazio 2002) for the 'average' visibility regime (Goodman & Narayan 1989; Taylor & Cordes 1993) for the line of sight to PKS 1954–388 ($l = 1.6°, ˜b = -29°$). Although the ISM has complex structure, and the NE2001 model cannot be used to reliably determine scattering properties along a particular line of sight, the result suggests that the intrinsic core size at 1.66 GHz might be significantly smaller than that measured, and the brightness temperature correspondingly higher.

However, as discussed by Johnson & Gwinn (2015), it is also necessary to consider the effect of refractive substructure introduced by scattering in the ISM. Refractive substructure has been seen in some RadioAstron pulsar observations (Gwinn et al. 2016; Popov et al. 2017) and may also be present in the RadioAstron observations of 3C 273 (Johnson et al. 2016). This can have the effect of enhancing detections on long baselines to RadioAstron, due to the appearance of fine-scale structure in the image of a resolved, scattered source, leading to an over-estimate of intrinsic brightness temperature.

We note that Pushkarev & Kovalev (2015) derive a median core size for PKS 1954–388 of 1.0 ± 0.2 mas at 2.3 GHz, and 0.35 ± 0.05 mas at 8.4 GHz, and a size-frequency dependence of $\nu^{-0.94\pm0.11}$, based on multi-epoch, simultaneous 2.3 and 8.4 GHz observations. Their results imply that intrinsic source size dominates over scatter-broadening at frequencies above 2.3 GHz. The upper limit to the angular size of 0.47 mas inferred from the RadioAstron observations of PKS 1954–388 is a factor of three times smaller than the angular size expected at 1.66 GHz from an extrapolation of the Pushkarev & Kovalev (2015) fit. The apparent discrepancy in core size measurement could be due to several factors: (i) the size of the core component may be time variable, as the flux density of the source is highly variable and was relatively low during the RadioAstron observations; (ii) the core component measured by Pushkarev & Kovalev (2015) resolves into several components at sub-mas angular resolution, implying the structure is more complex than accounted for by the simple circular Gaussian model-fitting of the sparse data; or (iii) the RadioAstron long baseline visibilities might be dominated by refractive noise. The observed correlated flux density seen on the RadioAstron baselines is at least ∼4% of the flux density of the compact component, which is considerably larger than the ∼1% RMS refractive noise predicted by Johnson & Gwinn (2015). In order to distinguish among the various possibilities, further RadioAstron observations on intermediate baselines less than 6 Earth-diameters are needed.

Although PKS 1954–388 is quite compact, has a flat radio spectrum and is very variable, as is seen in the light-curves in Figures 4 and 5, the lack of any rapid, large-amplitude intra-day or inter-day variability evident in ATCA monitoring in 2014 June (Section 3.3.1) means there is no observational evidence for the intra-day variability (IDV) often associated with scattering in the ISM. It is not yet possible to determine whether this is due to insufficiently compact structure in the source, or the lack of a nearby region of enhanced scattering along this line of sight, or both.

In any case, the detection of PKS 1954–388 on ∼80,000 km baselines at 1.6 GHz goes some way to vindicating the decision to place the satellite in an eccentric 9-d orbit, with apogee heights up to 350,000 km. The long space baselines provided by RadioAstron observations have enabled significantly higher brightness temperatures to be measured, e.g., in excess of 10^{13} K for 3C 273 (Kovalev et al. 2016), and the RadioAstron AGN Survey will extend these studies to a

much larger sample of sources (Kovalev et al., in preparation). The high sensitivity of the 18 cm receiver on board the RadioAstron Space Radio Telescope, in combination with large ground-based telescopes, is also leading to a new understanding of the effects of interstellar scattering.

4.2. Consideration of VLBI imaging

VLBI imaging to date has revealed the source to be strongly core dominated, with several weaker jet components. The multi-epoch monitoring of Piner et al. (2012) found evidence for two persistent components with apparent superluminal speeds. Extrapolating these motions, of ∼0.1 mas/yr, back to find an ejection epoch yields 1992.3 ± 2.4 for the inner component, and approximately 10 yr earlier for the outer component (Piner et al. 2012). These components are thus unlikely to be associated with the bright radio flares in 1996 (Tingay et al. 2003) and 2005–2006 (this paper). The extensive multi-epoch parsec-scale monitoring of AGN by the MOJAVE (Monitoring of Jets in Active galactic nuclei with VLBA Experiments) program demonstrated that, while there is some spread in the apparent speeds of separate features within an individual jet, there is support for the idea that there is a characteristic flow that describes each jet (Lister et al. 2009). Assuming, therefore, a similar motion for a component that might have emerged from the core in 1996, it would have been ∼1.2 mas from the core at the time of the first epoch TANAMI observation in 1998. It is interesting to note that there was indeed evidence for a component ∼1 mas from the core at that epoch. The TANAMI image from 2012 presented in this paper does not clearly resolve this component, which may be due to the slightly poorer east-west angular resolution at that epoch, or to this component merging with the inner of the two Piner et al. components. Any component ejected in 2005 would have been only 0.3 mas from the core in 2008 and 0.7 mas from the core in 2012 and so barely distinguishable from the core at these angular resolutions.

4.3. Connection between gamma-ray and radio flares

The short-term gamma-ray flares between 2009 and 2013 may have been accompanied by similar short-duration radio flares; however, our ATCA monitoring has not been sensitive to such short events. The much longer lived gamma-ray flare in 2013 is followed by a significant and extended flaring at radio energies. The characteristic brightening earlier, and more rapidly at higher frequencies is consistent with injection of a new population of high-energy electrons. There is a delay of approximately 9 months between the beginning of the gamma-ray outburst and the start of the radio flare.

Max-Moerbeck et al. (2014) cross-correlated 3-yr *Fermi* light-curves with 4-yr light-curves at 15 GHz, finding that only one of 41 sources with high-quality data in both bands shows correlations with significance larger than 3σ, demonstrating that great care is needed when comparing light curves even when many years of data are used. Thus, while it is a natural interpretation that the gamma-ray and radio flares are causally related, it is not possible to determine this unequivocally.

Fuhrmann et al. (2014) conducted a cross-correlation of radio and gamma-ray light-curves for 54 *Fermi* blazars, finding that the average source-frame time delay between gamma-ray and radio (with radio lagging) decreased from 76 ± 23 d at cm bands to 7 ± 9 d in mm/sub-mm bands, with this frequency dependence being in good agreement with jet opacity dominated by synchrotron self-absorption. The ATCA data shown in Figure 5 follow this trend, though the sampling is insufficiently frequent to assess this more quantitatively.

Similarly, Ramakrishnan et al. (2015) examined the discrete correlation function between radio and gamma-ray light-curves, finding that in most sources, the gamma-ray peaks lead the radio with time lags in the range 20–690 d. The ∼9-month delay between the onset of the gamma-ray and radio flares is thus quite consistent with these findings.

5 SUMMARY

The RadioAstron AGN Survey snapshot observation of PKS 1954–388 in 2012 detected the source on a 6.2 Earth-diameter baseline, confirming the presence of a compact core. A source frame brightness temperature of greater than 2×10^{12} K is implied, suggesting a minimum Doppler factor for the inverse Compton limit of 6. The simplest interpretation of the data yields a core size of 0.47 mas (in one dimension). If this is an over-estimate due to scattering in the ISM, a smaller core size and higher brightness temperature would be implied. On the other hand, refractive substructure can have the effect of enhancing detections on the long baselines to RadioAstron leading to an over-estimate of the brightness temperature. Further RadioAstron observations on baselines less than 6 Earth-diameters are needed to distinguish between the various possibilities.

ATCA monitoring shows that the source has varied by a factor of 5 in flux density at 8.4 GHz, and the *Fermi* light-curve suggests variations in the gamma-ray flux by a factor of at least 10. A radio outburst, rising earlier and faster at higher frequencies, followed a prolonged gamma-ray high state in 2013, with a lag between onsets of ∼9 months, comparable to that seen in other blazars. Multi-epoch VLBI observations reveal persistent jet components, with the innermost component in the first epoch TANAMI image plausibly associated with the 1996 radio outburst.

The multiwavelength data presented here were combined with other data to derive an SED, which was fitted using a one-zone synchrotron model. Despite the covariance between model parameters and the non-contemporaneous nature of the data, the model B fit yields a Doppler factor of ∼9, consistent with the lower limit to the inverse Compton Doppler factor of 6 inferred from the RadioAstron observation. The equipartition Doppler factor of at least 40 is much more difficult to reconcile.

ACKNOWLEDGEMENTS

The RadioAstron project is led by the Astro Space Center of the Lebedev Physical Institute of the Russian Academy of Sciences and the Lavochkin Scientific and Production Association under a contract with the Russian Federal Space Agency, in collaboration with partner organizations in Russia and other countries. The ATCA, Parkes and Mopra radio telescopes are part of the Australia Telescope National Facility, which is funded by the Commonwealth of Australia for operation as a National Facility managed by CSIRO. This study made use of data collected through the AuScope initiative. AuScope Ltd. is funded under the National Collaborative Research Infrastructure Strategy (NCRIS), an Australian Commonwealth Government Programme. This research was supported by Basic Research Program P-7 of the Presidium of the Russian Academy of Sciences. The *Fermi* LAT Collaboration acknowledges generous ongoing support from a number of agencies and institutes that have supported both the development and the operation of the LAT as well as scientific data analysis. These include the National Aeronautics and Space Administration and the Department of Energy in the United States, the Commissariat à l'Energie Atomique and the Centre National de la Recherche Scientifique/Institut National de Physique Nucléaire et de Physique des Particules in France, the Agenzia Spaziale Italiana and the Istituto Nazionale di Fisica Nucleare in Italy, the Ministry of Education, Culture, Sports, Science and Technology (MEXT), High Energy Accelerator Research Organization (KEK) and Japan Aerospace Exploration Agency (JAXA) in Japan, and the K. A. Wallenberg Foundation, the Swedish Research Council and the Swedish National Space Board in Sweden. Additional support for science analysis during the operations phase is gratefully acknowledged from the Istituto Nazionale di Astrofisica in Italy and the Centre National d'Études Spatiales in France. This research was funded in part by NASA through *Fermi* Guest Investigator grants NNH09ZDA001N, NNH10ZDA001N, NNH12ZDA001N, and NNH13ZDA001N-FERMI. T.H. was supported by the Academy of Finland project number 267324. Sasha Pushkarev is thanked for helpful discussions and Sara Buson is thanked for useful comments. This research has made use of NASA's Astrophysics Data System, and the NASA/IPAC Extragalactic Database (NED) which is operated by the Jet Propulsion Laboratory, California Institute of Technology, under contract with the National Aeronautics and Space Administration.

REFERENCES

Abdo, A. A., et al. 2010, ApJS, 188, 405
Abdo, A. A., et al. 2011, ApJ, 730, 101
Acero, F., et al. 2015, ApJS, 218, 23
Atwood, W. B., et al. 2009, ApJ, 697, 1071
Böck, M., et al. 2016, A&A, 590, A40
Böttcher, M., Mause, H., & Schlickeiser, R. 1997, A&A, 324, 395
Browne, I. W. A., Savage, A., & Bolton, J. G. 1975, MNRAS, 173, 87P
Burrows, D. N., et al. 2004, Proc. SPIE, 5165, 201
Cordes, J. M., & Lazio, T. J. W. 2002, arXiv:astro-ph/0207156
Fomalont, E. B., et al. 2000, ApJS, 131, 95
Fuhrmann, L., et al. 2014, MNRAS, 441, 1899
Gehrels, N., et al. 2004, ApJ, 611, 1005; erratum 2005, ApJ, 621, 558
Goodman, J., & Narayan, R. 1989, MNRAS, 238, 995
Gwinn, C. R., et al. 2016, ApJ, 822, 96
Hirabayashi, H., et al. 2000, PASJ, 52, 997
Impey, C. D., & Tapia, S. 1988, ApJ, 333, 666
Johnson, M. D., & Gwinn, C. R. 2015, ApJ, 805, 180
Johnson, M. D., et al. 2016, ApJ, 820, L10
Kalberla, P. M. W., et al. 2005, A&A, 440, 775
Kardashev, N. S., et al. 2013, ARep, 57, 153
Kellermann, K. I. 2002, PASA, 19, 77
Kellermann, K. I., & Pauliny-Toth, I. I. K. 1969, ApJ, 155, L71
Kovalev, Y. Y., et al. 2005, AJ, 130, 2473
Kovalev, Y. Y., et al. 2016, ApJ, 820, L9
Krauß, F., et al. 2016, A&A, 591, A130
Lister, M. L., et al. 2009, AJ, 138, 1874
Lobanov, A. 2015, A&A, 574, A84
Lovell, J. E. J., et al. 2013, JGeod, 87, 527
Max-Moerbeck, W., et al. 2014, MNRAS, 445, 437
Nolan, P. L., et al. 2012, ApJS, 199, 31
Ojha, R., et al. 2004, AJ, 127, 3609
Ojha, R., et al. 2010, A&A, 519, A45
Oshlack, A. Y. K. N., Webster, R. L., & Whiting, M. T. 2002, ApJ, 576, 81
Partridge, B., et al. 2016, ApJ, 821, 61
Petrov, L., Kovalev, Y. Y., Fomalont, E. B., & Gordon, D. 2011, AJ, 142, 35
Piner, B. G., et al. 2012, ApJ, 758, 84
Popov, M. V., et al. 2017, MNRAS, 465, 978
Pushkarev, A. B., & Kovalev, Y. Y. 2012, A&A, 544, A34
Pushkarev, A. B., & Kovalev, Y. Y. 2015, MNRAS, 452, 4274
Ramakrishnan, V., et al. 2015, MNRAS, 452, 1280
Readhead, A. C. S. 1994, ApJ, 426, 51
Roming, P. W. A., et al. 2004, Proc. SPIE, 5165, 262
Shakura, N. I., & Sunyaev, R. A. 1973, A&A, 24, 337
Shen, Z.-Q., et al. 1998, AJ, 115, 1357
Shimmins, A. J. 1971, AuJPA, 21, 1
Shimmins, A. J., Bolton, J. G., Peterson, B. A., & Wall, J. V. 1971, ApL, 8, 139
Stevens, J., et al. 2012, in Proc. Fermi & Jansky conference, arXiv:1205.2403
Taylor, J. H., & Cordes, J. M. 1993, ApJ, 411, 674
Tingay, S. J., et al. 2003, PASJ, 55, 351
Vercellone, S., Soldi, S., Chen, A. W., & Tavani, M. 2004, MNRAS, 353, 890
Wilson, W. E., et al. 2011, MNRAS, 416, 832